Research Square

Preprints are preliminary reports that have not undergone peer review.
They should not be considered conclusive, used to inform clinical practice,
or referenced by the media as validated information.

Analysis of Computed Tomography Image Features of Clear Cell Renal Cell Carcinoma on The Basis of Machine Learning: Differentiation of High-Grade from Low-Grade Fuhrman Nuclear Grades

Jenn Yeu Wang

nephrol@ms19.hinet.net

Taipei City Hospital

Chung-Ming Lo

National Chengchi University

Article

Keywords: Fuhrman nuclear grade, radiomic features, classifiers, Support vector machines, K Nearest neighbors, machine learning, clear cell renal cell carcinoma

Posted Date: November 16th, 2026

DOI: https://doi.org/10.21203/rs.3.rs-11364186/v1

License: This work is licensed under a Creative Commons Attribution 4.0 International License.
Read Full License

Additional Declarations: No competing interests reported.

Analysis of Computed Tomography Image Features of Clear Cell Renal Cell Carcinoma on The Basis of Machine Learning: Differentiation of High-Grade from Low-Grade Fuhrman Nuclear Grades

1. First and co- corresponding Author: Jenn Yeu Wang: Taipei City Hospital, Zhongxiao Branch; National Yang-Ming Chiao-Tong University; Fu Jen Catholic University; University of Taipei; Mackay Memorial College; Chihlee University of Technology; Taipei Medical University, Taiwan, R.O.C.; Chinese Culture University; National Chengchi University; National Normal University

2. Co-First author and corresponding Author: Chung-Ming Lo, National Chengchi University; Taipei Medical University, Taiwan, R.O.C. Telephone: 886-2-2736-1661 ext. 3345. Fax: 886-2-2739-2914,E-mail: buddylo@tmu.edu.tw

Equal contributions and credit given to Chung-Ming Lo and Jenn Yeu Wang:

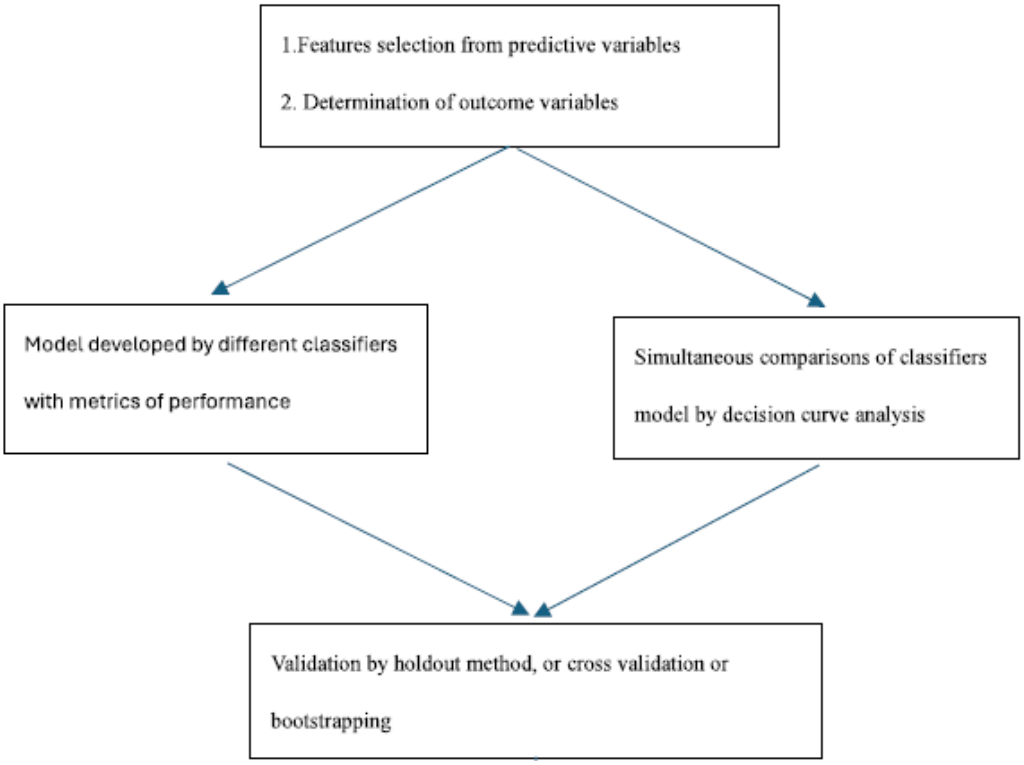
Word count :4585(not including table and figure)

Running title: Computed Tomography Texture Analysis and Fuhrman Nuclear Grades of Clear Cell Renal Cell Carcinoma

Correspondence:

Jenn-Yeu Wang, MD

1. 6F., No.3, Lane 36, Sec. 2, Hoping West Rd., Daan Dist., Taipei City 10662, Taiwan
2. Phone No.: 886-2-23633260; 886-2-910858991; 886-2-972751647
3. Fax No.: 886-2-23633260;
4. E-mail: nephrol@ms19.hinet.net



Graphic Abstract: Process of machine learning

Analysis of Computed Tomography Image Features of Clear Cell Renal Cell Carcinoma on The Basis of Machine Learning: Differentiation of High-Grade from Low-Grade Fuhrman Nuclear Grades

Chung-Ming Lo[5,6]; Jenn Yeu Wang[1, 2, 3, 4, 5, 6, 7, 8,]

[1]Taipei City Hospital, Zhongxiao Branch [2] National Yang-Ming Chiao-Tong University
[3] Fu Jen Catholic University [4] University of Taipei [5]National Chengchi University
[6]Taipei Medical University, [7]Mackay Memorial College; [8]Chihlee University of Taipei;

Abstract

Background: Previous researches have clarified potential clinical applications of radiomics-based prediction of tumor phenotype. The purpose of our research is to utilize radiomic features in computer-aided diagnosis (CAD) system of prediction for high Fuhrman nuclear grade and low Fuhrman nuclear grade in clear cell renal cell carcinoma (RCC)

Methods: We selected 110 images from 109 case number of axial contrast-enhanced computed tomography with a pathological diagnosis of clear cell RCC from The Cancer Imaging Achieve (TCIA) portal. After preprocessing and extraction of features of from radiological images, the Weka Experiment Environment was run to compare performance of different classifiers to predict high Fuhrman nuclear grade and low Fuhrman nuclear grade.
Results: Seventy features and 23 selected features were input into classifiers to predict high Fuhrman nuclear grade and low Fuhrman nuclear grade, respectively. The SVM based on poly-kernel classifier (Accuracy, sensitivity, specificity, area under the receiver operative characteristic curve (AUROC), precision, recall and F1 score were 82 %, 82%, 82%, 82%, 82%, 82% and 82 %, respectively) and K-Nearest neighbors (Accuracy, sensitivity, specificity, AUROC, precision, recall and F1 score were 90.91%, 91%, 89%, 90 %, 92%, 91 % and 91.5 %. Respectively) showed significant better performance than other classifiers, such as Bagging (Bagging), Naive Bayes (NaiveBayes), Boosting (AdaBoostM1), Decision trees (J48), Bayesian Network (BayesNet), library Support vector machines (LibSVM), Artificial Neural Networks (Multilayer Perceptron), Logistic regression (Logistic), Random Forest Tree (RandomForest),respectively.
Conclusions: The developed CAD system generated by the optimal machine-learning methods with radiomic features is a non-invasive method of predicting and monitoring tumor-nuclear grading characteristics in image-defined response evaluation in clinical practice of targeted therapy of clear cell RCC.
Key words: Fuhrman nuclear grade, radiomic features, classifiers, Support vector machines, K Nearest neighbors, machine learning, clear cell renal cell carcinoma

Abbreviation Table

Abbreviation Table

computer-aided diagnosis	CAD
renal cell carcinoma	RCC
area under the receiver operating characteristic	AUROC
anti-angiogenic agents	AAGs
vascular endothelial growth factor	VEGF
platelet-derived growth factor	PDGF
mammalian target of rapamycin	mTOR
The Cancer Imaging Archive	TCIA
computed tomography	CT
region of interest	ROI
Digital Imaging and Communications in Medicine	DICOM
bitmap	BMP
gray-level co-occurrence matrix	GLCM
normalized radius length	NRL
Support Vector Machine	SVM
Naive Bayes	NaiveBayes
Boosting	AdaBoostM1
Decision Trees	J48
K- Nearest Neighbors	IBk
Bayesian Network	BayesNet
Library Support Vector Machine	LibSVM
Artificial Neural Networks	Multilayer Perceptron
Logistic Regression	Logistic
Random Forest Tree	RandomForest
SVM classifiers with a sequential minimum optimization	SMO
SVM classifiers with a sequential minimum optimization based on poly-kernel	SMO poly-kernel
quantitative image biomarkers	QIBs
homogeneity matrix	homogeneityM
mean of grayscale values	MeanGray
variance of grayscale values	VarGray
skewness of grayscale values	SkewnessGray
kurtosis of grayscale values	KurtosisGray
average of normalized radial length	NRLAvg
standard deviation of normalized radial length	NRLSD

Introduction

There are approximately 338000 new patients of renal cancer globally in 2012. Renal cancer is currently the ninth most common cancer among adult male patients in the earth (214,000 patients), ranking fourteen most common cancer among adult female patients in the earth (124 000 patients). Renal cell carcinoma (RCC) contributes to more than 90% of renal cancer, of which clear cells (70%), papillary (10-15%) and chromophobe (5%) are the vast majority of histological types. About 2-3% of RCC are familial. The incidence of RCC is escalating and more common in developed countries and elderly population[1,2].

Although local RCC may be effectively managed by surgery or ablation, local or distant metastases and recurrence after management are not rare. Since recurrent disease could be successfully managed, monitoring of patients with RCC after management is very important. The monitoring protocol is usually developed from the comparison of size of the primary cancer at the time of the resection, the staging of tumor and the Fuhrman nuclear grades, size normalized standard deviation, reduction of contrast enhancement, entropy, uniformity, and when and where the new metastasis occurred [3-5]. Compared with other metastatic solid tumors, RCC metastases are abnormally rich in blood vessels. Current anti-angiogenic agents (AAGs) for blocking vascular endothelial growth factor (VEGF) and/or platelet-derived growth factor (PDGF) signaling pathways may be prescribed as first-choice or second-choice therapy for metastatic RCC. The use of mammalian target of rapamycin (mTOR) inhibitors to treat metastatic RCC is similar to these AAGs, by blocking the angiogenesis pathway of VEGF/PDGF and the cellular signaling pathway responsible for proliferation of tumor [1,4,5].

During successful AAGs treatment, the change of distribution of tumor blood

vessel, reduction of attenuation of contrast-enhanced computed tomography of tumor, staging of tumor, size of tumor, Fuhrman nuclear grades, and development of tumor necrosis on computed tomographic images are significant features and old criteria of prediction of successful AAGs treatment [6].

The use of contrast-enhanced computerized tomography to evaluate neo-vascularization is being used extensively in the detection and staging of cancer and in evaluating tumor response to treatment. The Fuhrman nuclear grade is a histopathological grading system routinely used for clear cell RCC worldwide. Currently, previous articles have demonstrated that histological grade 1 and grade 2 tumors classified as low-grade Fuhrman nuclear grades, and histological grade 3 and 4 tumors classified as high-grade Fuhrman nuclear grades would achieve better reproducibly and lower inter-observation variability, while retaining the overall prognostic value of survival [7]. This previous study also finds that there is no significance in distant metastasis between Fuhrman nuclear grade 1 or grade 2 in patients with clear cell RCC. Therefore, Fuhrman nuclear grade 3 and 4 tumors were used as index groups and grade 1 and 2 tumors as reference groups in our study.

At the present time, medical image analyses are ordinary and promptly available resources of medical information in clinical oncology. They can be used as cost-effective decision supports for targeted therapy of clear cell RCC[4,5]. Radiomics uses medical imaging data to customize cancer care, adding new and promising tools for precision oncology. In addition, medical image analysis can also predict intra-tumoral heterogeneity, which is generally thought as a main biomarker in oncology. Many studies have found that medical image analysis has established prediction models for different clinical variables (e.g., histological grade, survival, therapeutic response, etc.). A previous paper shows that computed tomography based radiomic image analysis

is highly accurate with 85.1% accuracy in the prediction of high-grade and low-grade Fuhrman nuclear grades in 54 images of clear cell RCC by the Support Vector Machine learning method compared with other 4 classifiers[8]. But little knowledge is about computed tomography based radiomic image analysis in the prediction of high-grade and low-grade Fuhrman nuclear grades in a larger cohort of clear cell RCC by experimental machine-learning methods (eleven classifiers). The current study developed CAD system of prediction of high-grade Fuhrman nuclear grades and low-grade Fuhrman nuclear grades in 100 images of clear cell RCC by experimental machine-learning methods for the health care providers as an aid in decision making of treatment response of tumors.

Materials and Methods

The study received a grant from Health of Department of Taipei City Government with the case number of 10801-62-054. The project entitled with "Analysis of Different Types Clear Cell Carcinoma Based on Computerized Tomography Texture Analysis and Machine Learning" was approved by Research Ethics Committee of the Taipei City Hospital on November 7, 2018 with the case number TCHIRB-10710117-W.

Patient Information

The Cancer Imaging Archive (TCIA)

This study was a retrospective case-control study. Patients with clear cell RCC were collected by recruiting the abdominal imaging database of The Cancer Imaging Archive (TCIA) (http://cancerimagingarchive.net/) of the National Cancer Institute, a website registering images of The Cancer Genome Atlas (TCGA) patients for medical image analysis. The images and data recruited by TCIA were utilized to comply with every related policy, regulation, and law for the protection of patients. Every essential

agreement, authorization, human right guarantee, informed consent record, and written agreement of institutional review boards was received (http://cancerimagingarchive.net/). Prior to receiving any form of treatment, every patient with clear cell RCC underwent axial computed tomography (CT) scan. In the current study, we included 109 patients with 110 diagnostic contrast-enhanced axial computed tomographic images from the TCIA data portal (mean age 59.55 ± 12.39, with a female to male ratio of 38: 71).The pathological stages of these 109 patients are as follows: stage I, 60 patients; stage II, 7 patients; stage III, 25 patients; stage IV, 17 patients .Fuhrman nuclear grades of these 110 image are described as the following: grade 1, 1 image; grade 2, 49 images; grade 3, 34 images; grade 4, 26 images. The race distribution of these 109 patients is showed as follows: Asian, 2 patients; Black, 4 patients; White, 103 patients. Among these 109 patients, 51 clear cell RCC arose from left kidney and 58 clear cell RCC were found in right kidney.

Image Analysis

Contrast-Enhanced Axial CT Images

In this study, we included the 110 contrast-enhanced CT images from 109 patients of the TCIA data portal. Contrast-enhanced axial abdominal computed tomography images were recruited for analysis in our study. A board-qualified nephrologist, Wang Jenn Yeu with about 19 years of practicing experience and blinded to the clinical and pathological information, chose the most heterogeneous two-dimensional slice with maximum tumor area from a sequence of contrast- enhanced CT axial images [Figure1and Figure 2]. A solid tumor graph with the highest part of necrosis, which defined as hypo-attenuated, non-contrast enhancing areas which were not sharply delineated and were lacking in obvious margins was chosen on axial contrast-

enhanced CT scans [9]. Drawing contour of the most heterogenous tumor was then manually done by using image J on the axial contrast-enhanced abdominal computed tomography [Figure 2]. To minimize the partial volume effect due to surrounding structure, the drawing line was meticulously contoured when trying to keep an about distance of 2–3 mm within the edges of tumor. Pixels inside the region of interest (ROI) of tumor were utilized for further medical image analysis. The images were anonymized and stored as bitmap (BMP) files. Flowchart of medical image analysis was shown in Figure 3.

Preprocessing

The CT images were transformed into the standard medical digital graph communication protocol, namely DICOM (Digital Imaging and Communications in Medicine) for storage in the computer. After the auxiliary system was read and converted to BMP file, it was processed in 8-bit gray scale (0 ~ 255). Subsequent image processing was described as follows. The images were reviewed on a sequence of images using the Image J software. All regions of interest were obtained in the axial plane. These images were stored in a server and portable hard drives. The pre-processing involves filtering, normalization, segmentation, and object identification.

Radiomic Features Extraction.

Feature extraction was performed using a technique known as moment for distribution of grayscale values, Gray-level co-occurrence matrix (GLCM), and Gabor filters with the use of MATLAB R2016b (The MathWorks, Natick, MA). These radiomic features on axial contrast- enhanced computed tomography images were separated into four feature groups: I) intensity features, II) shape features, III) GLCM

texture features and IV) Gabor wavelet transformation texture features [Table1]. Intensity features evaluate the first order statistics of the pixel intensity histogram, while shape features depict the two-dimensional properties of the axial abdominal computed tomography images of tumor. Gray-level co-occurrence matrix (GLCM) texture features quantify the intra-tumor heterogeneity. Wavelet features are the transformed domain description of the intensity and texture features. In addition to the extraction methods, mathematical definitions of all radiomic features have been previously described [10].

Morphological Features

After contouring the region of interest (ROI) of the tumor using the software image J on contrast-enhanced axial computed tomography images, we used an algorithm to automatically segment the contour of the tumor, calculate the perimeter of the ROI, and also calculated the area of the ROI. The 5 morphology features proposed in the text were as follows: perimeter of the ROI, area of the ROI, compactness of ROI and average and standard deviation of the normalized radius length (NRL) for the ROI. The equations for calculating the compactness, the mean (μ) and standard deviation (σ) of the normalized radial length (NRL) line graph are as follows:

$$C=4\pi A/P^2$$

$$\mu_{NRL} = \frac{1}{N}\sum_{i=0}^{N-1} r_i$$

$$\sigma_{NRL} = \sqrt{\frac{1}{N}\sum_{i=0}^{N-1}(r_i - \mu_{NRL})^2}$$

Where P is the perimeter of the ROI and A is the area of the ROI. C represents the compactness, C value increases as the complexity of the shape of the ROI increases, which is due to concave or protruding parts. If the ROI is round, the

ratio is close to 1. Where r_i is the value of the normalized radial length of the boundary coordinates (X *i*, Y *i*), the μ_{NRL} is the average of normalized radial length line graph, and σ_{NRL} is the standard deviation of the normalized radial length line plot of the i_{th} tumor. The average of normalized radial length and its standard deviation are measures of how the boundary changes in a macroscopic way, similar to circularity, but can also represent fine boundary variations. The normalized radial length (NRL) is defined as the Euclidean distance of the pixels from the center of the ROI to the pixels of each edges of the ROI and then normalized to the maximum radius[11].

Intensity Features

The pixel values of gray scale of the ROI of tumor were represented by a histogram. A histogram is a graph distribution that calculates the number of happenings of each pixel values of gray scale and then plots it based on the frequency of happenings. The horizontal axis is pixel values of gray scale, the range is 0 to 255, and the vertical axis is the frequency of occurrences. The quantitative moment of pixel values of gray scale distributions for the ROI were calculated that the central moments of the histogram were increased to the power of one, two, three, and four, namely mean, variance, skewness, and kurtosis:

$$\text{Mean} = \frac{1}{N}\sum_{i=1}^{N} P_i,$$

$$\text{Variance} = \frac{1}{N}\sum_{i=1}^{N} (P_i - Mean)^2,$$

$$\text{Skewness} = \frac{1}{N}\sum_{i=1}^{N} (P_i - Mean)^3,$$

$$\text{Kurtosis} = \frac{1}{N}\sum_{i=1}^{N} (P_i - Mean)^4,$$

where P_i is the intensity of pixels values, and N is the number of pixels values. The

mean represents the mean of pixel values of gray scale of the ROI. Variance represents the sum of the squared values of the subtraction of the pixel values of gray scale from the average pixel values of gray scale of each pixel. Skewness is used to measure the asymmetry of pixel values of gray scale distribution. The coefficient of right skewness is greater than zero and the distribution is more concentrated on the left. The coefficient of skewness of normal distribution is equal to zero, the distribution is symmetrical, and the mean is equal to the median value. For the left skewness, the coefficient is less than zero and the distribution is skewed to the right. The kurtosis is used to measure the sharpness of the peak of the pixel values of gray scale distribution [12]. In case of normal distribution, the coefficient of kurtosis is 3. If the kurtosis of a distribution is higher than normal distribution, the coefficient of kurtosis is greater than 3. In case of kurtosis of a distribution lower than normal distribution, the coefficient of kurtosis is lower than 3.

Gray- Level Co-occurrence Matrix Texture Features

The texture is a phenomenon that describes the spatial relationship between the tone primitives or groups of similar pixels in the ROI. The distance between each pixel and the neighboring pixels is d, while the angles are θ. After computing the number of co-occurrences of pixels and neighboring pixels, a new matrix called gray-level co-occurrence matrix (GLCM) is produced by converting the data of the common frequency. Variable statistics of GLCM texture features is calculated by computing the relationship and variation of the GLCM.

The gray- level co-occurrence matrix is kept in an $i \times j \times n$ matrix, where n is the number of GLCM typically calculated because of the different orientations and displacements utilized in the algorithm. In general, the values i and j are equal to the 'NumLevels' parameters of GLCM calculation function graycomatrix (). Notice that, as

provided in some references, MATLAB calculation values belong to the set {1, ..., NumLevels} instead of {0,..., (NumLevels-1)}. Although in the MATLAB image processing toolbox, graycoprops() can calculate the GLCM four functions (contrast, correlation, energy, and homogeneity).Besides, MATLAB can calculate more GLCM functions, such as autocorrelation, contrast, correlation, cluster prominence, cluster shade , dissimilarity, energy, entropy, homogeneity, homogeneity matrix, maximum probability, sum of squares: sum average, sum variance, sum entropy, difference variance, difference entropy, information measure of correlation I, information measure of correlation II, information measure of correlation ii, inverse difference normalized, inverse difference moment normalized[13].

Gabor Wavelet Transformation Texture Features

Since Dennis Gabor proposed combined basic functions to represent signals in 1946, Gabor functions have been deployed in many areas of signal processing. The two-dimensional Gabor function has been used to simulate a good model system of simple cells in mammalian visual sensory cortex and is commonly used to detect edge. The invariance of position, ratio and direction of the ROI are detected in the Gabor wavelet transformation texture feature space. When Gabor filter is used for feature extraction, it has advantage of the invariance of time to frequency information, shiftability, and redundant wavelets. In recognition of two-dimensional patterns, the invariant characteristics of illumination, orientation, scale, and translation are the most typical requirements. Although Gabor filter has invariance in moment, it needs precise segmentation and uniform lightening [14,15].

The first function constitutes a customized Gabor filter bank. It invents a *u* by *v* cell array, whose elements are *m* by *n* matrices; each matrix is a two-dimensional Gabor filter. The second function takes Gabor wavelet transformation texture features

from the input image. It invents a column vector that consists of the Gabor wavelet transformation texture features of the input image. The feature vector normalizes to zero mean and unit variance. At the final part of each file, there is a display portion that draws the filter and displays the filtered image. The Gabor wavelet pyramid is a filter bank that spatially orients a sinusoid grating by a Gaussian window. The Gabor filter uses a custom scale at all possible positions within the f x f grid, where f is the spatial frequency. Minimum spatial frequency is set to one cycle per base scale. Tails of Gabor wavelets are truncated by self-defined thresholds to limit the scope. The Gabor filters are z scored in their non-truncated range.

Features Selection

Feature selection techniques may help identify the most prominent radiomic features predicting high-grade Fuhrman nuclear grades and low-grade Fuhrman nuclear grades. First, the conventional approach of feature selection algorithm is as follows: The Kolmogorov-Smirnov test was initially utilized to evaluate normality of these 70 radiomic features. Two independent sample *t*-test was then chosen to evaluate the features with normal distributions, whereas others without normal distributions were evaluated by the Mann-Whitney U-test. P values < 0.05 was chosen at a significant level.

Classifiers.

Given that kernel values generally rely on the products of inside feature vectors, e.g., the linear kernel and the polynomial kernel, big attribute values may result in numerical problems. Scaling before applying Support Vector Machine (SVM) is very important, but we found that no significant better accuracy when all the features are normalized to have zero mean and unit variance. In our study, we used 11 machine-learning classifiers (relevant acronyms) including Bagging, Naive Bayes

(NaiveBayes), Boosting (AdaBoostM1), Decision Trees (J48), K- Nearest Neighbors (IBk), Bayesian Network (BayesNet), Library Support Vector Machine (LibSVM), Artificial Neural Networks (Multilayer Perceptron), Logistic Regression (Logistic), Random Forest Tree (RandomForest), and Support Vector Machine based on poly-kernel (SMO-poly-kernel). Every classifier was implemented in WEKA Experiment Environment using WEKA version 3.8.2. Classifiers were trained using the split sample validation of training group (90% data set) and their predictive performances were assessed in the validation group (10% data set) using accuracy, sensitivity, specificity, precision, area under receiver operating characteristic (AUROC) curve and recall.

Statistical Analysis

The datasets were divided into the following two parts: First, experimental factors based on high-grade nuclear grades and low-grade nuclear grades prediction(class), Second, radiomic features(attributes). Before performing machine learning, we discovered that the accuracy of SVM classifier based on poly-kernel was higher than that of radial base function; and we also found that there were no differences in the accuracy of prediction by optimized parameters and default values of the SVM classifier. Therefore, we used SVM classifier based on poly-kernel with default values of parameters when we ran Weka software version 3.8.2 Experiment Environment [16]. The performance evaluation was done to separate the low-grade Fuhrman nuclear grades from high- grade Fuhrman nuclear grades. Predictive performance of each classifier was assessed using accuracy (percent correct), sensitivity (true positive rate), specificity (true negative rate), recall, precision and area under receiver operating characteristic (AUROC) curve. To successfully implement predictive analysis based on medical images, we evaluated and compared 11 machine learning

classifiers. Practical machine learning tools and techniques including heterogenous ensembles, such as Bagging (Bagging), Boosting (AdaBoostM1), Random Forest Tree (RandomForest), and homogenous ensembles, such as Naive Bayes(NativeBayes), Decision Trees (J48), K- Nearest Neighbors (IBk), Bayesian Network (BayesNet), Artificial Neural Networks (Multilayer Perceptron), Logistic Regression(Logistic), Library Support Vector Machine (LibSVM) and SVM classifiers with a sequential minimum optimization based on poly-kernel (SMO poly-kernel).To investigate and compare the 11 classification methods, we used paired T test. For each classifier, we trained the model on the sub-sampled training group (size 90%) and validated the performance on the validation group (size 10%).

Results

Before implementation of the machine-learning approaches, a total of 70 radiomic features were harvested from the contoured tumor regions of the contrast on enhanced axial computed tomography images. These radiomic features contained 4 histogram features (mean, skewness, kurtosis and variances), 21 grey-level co-occurrence matrix texture features, 5 shape features and 40 Gabor wavelet transformation features [Table 1]. Definitions and mathematical equations for these radiomic features have been demonstrated in previous studies [10-15]. Table 2 shows the significant 23 radiomic features, tested by either Student's t-test (with a normal distribution) or the Mann-Whitney U-test (with a non-normal distribution), and the corresponding p values.

Predictive Performance of Classifiers

Using 23 selected features, we showed K-Nearest Neighbor classifier had significant better performance than other 10 classification methods, and sensitivity, specificity, accuracy, precision, recall and AUROC curve were 91%, 89%, 90.91 %,

92 %, 91% and 90%, respectively. Table 3 displays the performance of classification methods using 23 selected features. Using 70 extracted features, the SVM classifier showed significant better performance, and sensitivity, specificity, accuracy, precision, recall and AUROC curve were 82%, 82%, 81.82%, 82%, 82% and 82%, respectively. The details of equations of computed tomography texture features were shown in Table 4.

Discussion

Among these 109 patients having pathological diagnosis of clear cell RCC, 50 images with Fuhrman nuclear grade 3 and 4 were defined as high- grade Fuhrman nuclear grades, and 60 images with Fuhrman nuclear grade 1 and 2 defined as low-grade Fuhrman nuclear grades. Extracted radiomic image features were classified into four groups: I) intensity features(N=4), II) shape features(N=5), III) GLCM texture features(N=21), and IV) Gabor wavelet transformation texture features(N=40). The accuracy of K-Nearest Neighbors classifier on 23 relevant features by using feature selection method with analysis of normality tested by either independent sample t test (with a normal distribution) or Mann-Whitney U test (without a normal distribution) got the highest accuracy (91 %) in prediction of high-grade Fuhrman nuclear grades and low-grade Fuhrman nuclear grades. In addition, SVM classifiers on 70 radiomic image features also fetched not bad accuracy (81.82%) in the prediction of high-grade Fuhrman nuclear grades and low-grade Fuhrman nuclear grades. In addition to variance and mean of grayscale values, shape features (area and perimeter) were highly statistically significant for discrimination of high-grade and low-grade Fuhrman nuclear grades of clear cell RCC in our study [Table 2].

Tumor heterogeneity (for example, variation in nuclear size or chromatin texture),

being quantified by karyomeric analysis, describes the genetic and epigenetic differences between cancer cells within the same type of tumor. Because of tumor heterogeneity, cancer clones have different molecular characteristics, sensitivity to treatment and prognosis [17]. Therefore, exploring how to accurately assess tumor heterogeneity clinically is essential for the development of effective personalized therapy and evaluation of different responses to treatment. A previous paper showed that the imaging pattern of attenuation characteristics and enhancement properties of cross-sectional computed tomographic images could discriminate high-grade and low-grade Fuhrman nuclear grades [18].

With the development of anti-cancer therapies targeting specific molecular pathways, it has become crucial to develop methods to assess the response of these targeted drugs to cancer treatments. Although image features of computed tomography scans and magnetic resonance image are useful in many situations, there is increasing evidence that traditional image features cannot accurately assess cancer heterogeneity and cannot accurately predict response of targeted drugs to cancer treatments. Deployment of standardized quantitative medical imaging techniques are promising to personalize management of cancer patients and are as follows [Figure 3]: 1. medical image pre-processing, 2. image feature extraction and selection, 3. providing scientific and clinically relevant data, 4. establishing a machine learning classifier model to best accurately predict high-grade and low- grade Fuhrman nuclear grades

In this study, SVM classifiers with a sequential minimum optimization (SMO) algorithm was used to perform a not bad accurate classification rate while using 70 extracted features. The main advantage of the sequential minimum optimization algorithm is that it can quickly solve the quadratic equation problem without the need

for additional matrix storage, or iterative numerical routine for each sub-problem. The basic SVM is characterized as a supervised machine learning algorithm that can solve linear and nonlinear classification problems, and as a feed forward neural network that is considered to have only one hidden layer. The main idea of the SVM classifier is that decides hyperplane separate instances and maximizes the boundaries between different classes. Support Vector Machine classifiers own several notable features that make them particularly suitable for structure activity relationships and quantitative structure activity relationships applications. First, the structure activity relationships model based on the SVM has the greatest separation between the two categories that must be distinguished. Second, SVM converts input space into feature space based on special kernel functions. Hyperplanes can separate categories that are hard or even impractical to differentiate in the input space. Third, a particular character of the kernel function allows the SVM model to be calculated based on the input space description equation without the need to explicitly evaluate the feature space. Fourth, the SVM model has a specially good solution for a known kernel function and connected parameters, this kernel function significantly reduces the numerical complexity [19].

In our study, K- Nearest Neighbors classifier was used to perform the highest accurate classification rate on 23 selected extracted features. The K-Nearest Neighbors classifier presents the classification of any pre-classified data on the two-dimensional coordinates associated with the classification of the kth neighbors to the nearest distance. The K-Nearest Neighbors classifier easily allows risk information to be presented in a manner that specifies the rejection regions. The K-Nearest Neighbors classifier details two error estimation methods, namely the error counting technique and the risk averaging method. It is generally stated that the result of the K-

Nearest Neighbors classifier is the standard majority vote classifier. In addition, the Nearest Neighbor classifier characterizes as a nonparametric classifier and centralized algorithm for the nearest distance error count for any pre-classified data. The K-Nearest Neighbors classifier can be graphically displayed the nearest distance relationship of the pre-classified data. The K -Nearest Neighbors classifier can represent the smallest error, the least cost, most intuitively among all classifiers [20].

Heterogeneity of tumor vessels is a discernible feature of malignant tumors. Image analysis of contrast-enhanced computed tomography is a medical image processing method quantifying this heterogeneity of tumor vessels by assessing texture features. By using a series of changes in quantitative image biomarkers (QIBs), previous papers showed that the relative changes of heterogeneity can be only evaluated by entropy and uniformity [4,5,21]. Uniformity reflects the distribution of grayscales in tumors, such as mean of positive pixels, standard deviation of the pixel distribution histogram[21], and mean or variance of grayscale values (highly statistically significant in our study). Higher entropy and lower consistency indicate increased tumor heterogeneity. Besides quantitative image biomarkers (QIBs), such as variance and mean of grayscale values, shape features (such as area and perimeter), we developed highly accurate and trusty machine learning methods to facilitate the successful prediction of high-grade and low-grade Fuhrman nuclear grades in clinical radiographic imaging applications and to highlight for individualized target therapy in patients with clear cell RCC.

Our research demonstrated a highly accurate machine learning approach for identifying low-grade and high-grade Fuhrman nuclear grades in clear cell renal cell carcinoma, which added a piece of information in computer aided diagnosis for treatment response to target therapy. The highly significant computed tomography-

based features, such as variance and mean of grayscale values, shape features (area and perimeter), also supported usefulness of the current radiomic biomarkers (size normalized standard deviation, entropy, uniformity, mean of positive pixels, and standard deviation of the pixel distribution histogram).

Conclusion

Our study demonstrated that computed tomographic radiomics-based biomarkers can accurately discriminate between high and low Fuhrman nuclear grades in clear cell renal cell carcinoma with holdout validation. In other words, this study demonstrates that interpretable machine learning models combined with CT-derived imaging features can effectively predict preoperative Fuhrman nuclear grading of clear cell renal cell carcinoma (ccRCC). The model demonstrates good performance and interpretability, providing a promising non-invasive tool for personalized clinical decision-making. Larger, multicenter studies are needed in the future to validate and expand these findings, paving the way for clinical applications.

Limitation: This research with a small sample size machine learning model development introduces validation challenges, further multicenter designs, external generalizability may significantly diminish this disadvantage

Declarations

• **Ethics approval and consent to participate**--

Because of this study is a study using open access image data, the consent of participate was waived. The project entitled with "Analysis of Different Types Clear Cell Carcinoma Based on Computerized Tomography Texture Analysis and Machine Learning" was approved by Research Ethics Committee of the Taipei City Hospital on November 7, 2018 with the case number TCHIRB-10710117-W.

Our manuscript only used already anonymized images files of TCIA portal and does not report on or involve the use of any animal or human data or tissue, this section is not applicable to your submission.

•**Consent for publication--** Our manuscript did not contain any individual person's data in any form (including individual details, images or videos), consent to publish

was waived. Our manuscript does not contain any individual person's data, consent to publish is not applicable in this section.

• **Data Availability Statement** - All data supporting the findings of this study are available within the paper and its Supplementary Information. In the data ecosystem of The Cancer Imaging Archive (TCIA), "UUID Generator" is typically associated with data de-identification. Anonymized data with UUID supporting the results reported this published article can be found in TCIA portal under the request from the authors.

•**Competing interests--** All authors have no conflict of interests to declare.

• **Funding** - The study received a grant from Health of Department of Taipei City Government with the case number of 10801-62-054.

•

• **Acknowledgements--**The authors thank Department of Health, Taipei City Government provision of grant. Besides, the authors also thank Taipei City Hospital Research Ethics Committee for approval of the study.

Table 1 Description of extracted features (abbreviation)

Types of Features	Features and Abbreviations
Gray-level co-occurrence matrix (GLCM) texture features(N=21)	contrast, correlation, cluster prominence, cluster shade, dissimilarity, energy, entropy, homogeneity, difference variance, difference entropy, information measure of correlation I, inverse difference normalized, inverse difference moment normalized, autocorrelation, maximum probability, sum of squares, sum average, sum variance, sum entropy, information measure of correlation II, homogeneity matrix (homogeneityM)
Intensity features(N=4)	mean of grayscale values (MeanGray), variance of grayscale values (VarGray), skewness of grayscale values (SkewnessGray), kurtosis of grayscale values (KurtosisGray)
Shape features (N=5)	area, perimeter, compactness, average of normalized radial length (NRLAvg), standard deviation of normalized radial length (NRLSD)
Gabor wavelet transformation texture features (N=40)	Gabor wavelet transformation texture features 1-40 (Gabor 1-40)

Table 2 Significant radiomic features and relevant p values generated by independent sample t test (normal distribution) or Mann Whitney U test (non-normal distribution)

Features	Low- grade Fuhrman nuclear grades (N=50)		High-grade Fuhrman nuclear grades(N=60)		P value
	Mean± SD	Median	Mean± SD	Median	
Autocorrelation	28.83±4.85		26.47±5.63		0.022
Contrast		1.49		1.06	0.002
Correlation		0.87		0.90	0.016
Sum of squares	29.49±4.83		26.96±5.83		0.016
Sum average	9.76± 0.91		9.29±1.12		0.019
Sum variance	81.93±17.37		74.48±19.19		0.037
Difference variance		1.49		1.06	0.002
Inverse difference moment normalized		0.98		0.99	0.004
Mean of grayscale values		5.17		12.25	<0.001
Variance of grayscale values		61.00		398.57	<0.001
Area		1322.50		3137.00	<0.001
Perimeter		124.00		195.00	<0.001
Gabor 10		-0.08		-0.82	0.01
Gabor11		0.36		-0.52	0.038
Gabor12		-0.39		-0.77	0.048
Gabor18		0.16		-0.61	0.016
Gabor20		0.02		-0.65	0.011
Gabor25	-0.56± 0.81		-0.89±0.75		0.027
Gabor 26		0.49		-0.32	0.01
Gabor28		0.30		-0.17	0.01
Gabor29		-0.51		-0.99	0.007
Gabor33	-0.92±0.71		-1.23±0.68		0.024
Gabor37	-0.87±0.68		-1.14±0.66		0.036

Table 3. Performance of eleven classifiers for prediction of high-grade and low-grade Fuhrman nuclear groups for selected 23 features

Types of classifiers	TPR	TNR	Percent correct	Recall	Precision	AUROC
BayesNet	0.64	0.63	63.64	0.64	0.64	0.70
NaiveBayes	0.64	0.66 v	63.64	0.64	0.67 v	0.57 *
LibSVM	0.55 *	0.45 *	54.55 *	0.55 *	-	0.50 *
Logistic	0.64	0.63	63.64	0.64	0.64	0.60 *
MultilayerPerceptron	0.64	0.63	63.64	0.64	0.64	0.53 *
SMO-poly-kernel	0.64	0.63	63.64	0.64	0.64	0.63 *
IBk	0.91 v	0.89 v	90.91 v	0.91 v	0.92 v	0.90 v
AdaBoostM1	0.64	0.60 *	63.64	0.64	0.64	0.65 *
Bagging	0.64	0.60 *	63.64	0.64	0.64	0.53 *
J48	0.64	0.60 *	63.64	0.64	0.64	0.57 *
RandomForest	0.73 v	0.71 v	72.73 v	0.73 v	0.73 v	0.80 v

Abbreviations: v, significant better; *, significant worse; -, cannot be computed by WEKA; TPR, true positive rate; TNR, true negative rate; AUROC, area under receiver operating characteristic curve; GLCM, Gray-level co-occurrence matrix; AdaBoostM1, Boosting; RandomForest, Random Forest Tree; NaiveBayes, Naive Bayes; J48,
Decision trees; IBk, K- Nearest Neighbors; BayesNet, Bayesian Network; Multilayer Perceptron, Artificial Neural Networks; Logistic; Logistic Regression; SMO-poly-kernel, Support Vector Machine based on poly-kernel.

Table 4

Features (abbreviation)	Equation
Mean of grayscale value (MeanGray)	$\frac{1}{N}\sum_{i=1}^{N} pi$
Variance of grayscale value (VarianceGray)	$\frac{1}{N}\sum_{i=1}^{N} (pi - MeanGray)^2$
Skewness of grayscale value (SkewnessGray)	$\frac{1}{N}\sum_{i=1}^{N} (pi - MeanGray)^3$
Kurtosis of grayscale value(KurtosisGray)	$\frac{1}{N}\sum_{i=1}^{N} (pi - MeanGray)^4$
Area(A)	πr^2
Perimeter(P)	$2\ \pi r$
Compactness	$\frac{4\pi A}{P2}$
Average of normalized radial length(NRLavg)	$\frac{1}{N}\sum_{i=0}^{N-1} ri$

Standard deviation of normalized radial length(NRLSD)	$\sqrt{\frac{1}{N}\sum_{i=0}^{N-1}(ri - \mu_{NRLavg})}$
Autocorrelation	$\sum_i \sum_j (p_x \mu_x)(p_y \mu_y)/\sigma_x \sigma_y$
Contrast	$\sum_n n^2 \{\sum_i \sum_j p(i-j)\}. \quad \lvert i-j \rvert = n$
Correlation	$\sum_i \sum_j (i-\mu_x)(j-\mu_y)p(i,j)/\sigma_x \sigma_y$
Cluster prominence	$\sum_i \sum_j (i + j - \mu_x - \mu_y)^4 p(i,j)$
Cluster shade	$\sum_i \sum_j (i + j - \mu_x - \mu_y)^3 p(i,j)$
Dissimilarity	$\sum_i \sum_j p(i,j)\lvert i-j \rvert$
Angular second moment(Energy)	$\sum_i \sum_j p(i,j)^2$
Entropy(HXY)	$-\sum_i \sum_j p(i,j)\log(p(i,j))$

homogeneity matrix	$-\sum_i \sum_j \frac{1}{1+i-j} p(i,j)$
Difference variance	$\sum_i i^2 \; p_{x-y}(i)$
Difference entropy	$-\sum_i p_{x-y}(i) \log\{p_{x-y}(i)\}$
Information measure of correlation 1	$\frac{HXY-HXY1}{max\{HX,HY\}}$ $HXY=-\sum_i \sum_j p(i,j)\log\{(p(i,j))\}$ $HXY1=-\sum_i \sum_j p(i,j)\log(p_x(i)\,p_y(j))$ where HX, HY are entropies of P_x and p_y
Information measure of correlation 2	$(1\text{-}\exp[-2.0(HXY2\text{-}HXY])^{1/2}$ $HXY2=-\sum_i \sum_j p_x(i)p_y(j)\log\{p_x(i)\,p_y(j)\}$
Inverse difference normalized	$\sum_i \sum_j \frac{1}{1+\lvert i-j\rvert Ng} p(i,j)$
Inverse difference movement (homogeneity)	$-\sum_i \sum_j \frac{1}{1+(i-j)2} p(i,j)$

Sum of squares	$\sum_i \sum_j (i-\mu)^2 p(i,j)$
Sum average	$\sum_{i=2}^{2Ng} i\, p_{x+y}(i)$
Sum variance	$\sum_{i=2}^{2Ng} (i\text{-SE})^2\, p_{x+y}(i)$ $SE = -\sum_{i=2}^{2Ng} p_{x+y}(i) \log\{p_{x+y}(i)\}$
Sum entropy(SE)	$-\sum_{i=2}^{2Ng} p_{x+y}(i) \log\{p_{x+y}(i)\}$
Maximum probability	$\max\ p(i,j)$
Inverse difference movement normalized	$-\sum_i \sum_j \frac{1}{1+(i-j)2/Ng} p(i,j)$
Gabor transformation texture features(Gabor feature) Gabor 1-40 are created by 5 scales and 8 orientations	$g(x,y;\lambda,\theta,\varphi,\sigma,\gamma) = \exp\left(\frac{-x'^2+\gamma^2y'^2}{2\sigma^2}\right)\exp\left(i\left(2\pi\frac{x'}{\lambda}+\varphi\right)\right)$ $g_{real}(x,y;\lambda,\theta,\varphi,\sigma,\gamma) = \exp\left(\frac{-x'^2+\gamma^2y'^2}{2\sigma^2}\right)\cos\left(i\left(2\pi\frac{x'}{\lambda}+\varphi\right)\right)$ $g_{imag}(x,y;\lambda,\theta,\varphi,\sigma,\gamma) = \exp\left(\frac{-x'^2+\gamma^2y'^2}{2\sigma^2}\right)\sin\left(i\left(2\pi\frac{x'}{\lambda}+\varphi\right)\right)$ where $x' = x\cos\theta + y\sin\theta$ and $y' = -x\sin\theta + y\cos\theta$

Produced by Jenn Yeu Wang, MD, MS

For GLCM texture features

$p(i, j/d, \theta)$ *represent the frequency of two surrounding pixels* (i, j) *in a distance* d *and a direction* θ.

μ_x, μ_y, σx, *and* σy are mean and standard deviation of the distributions of $p(i, j/d, \theta)$,

$$\mu_x = \sum_i i \sum_j p(i, j)$$

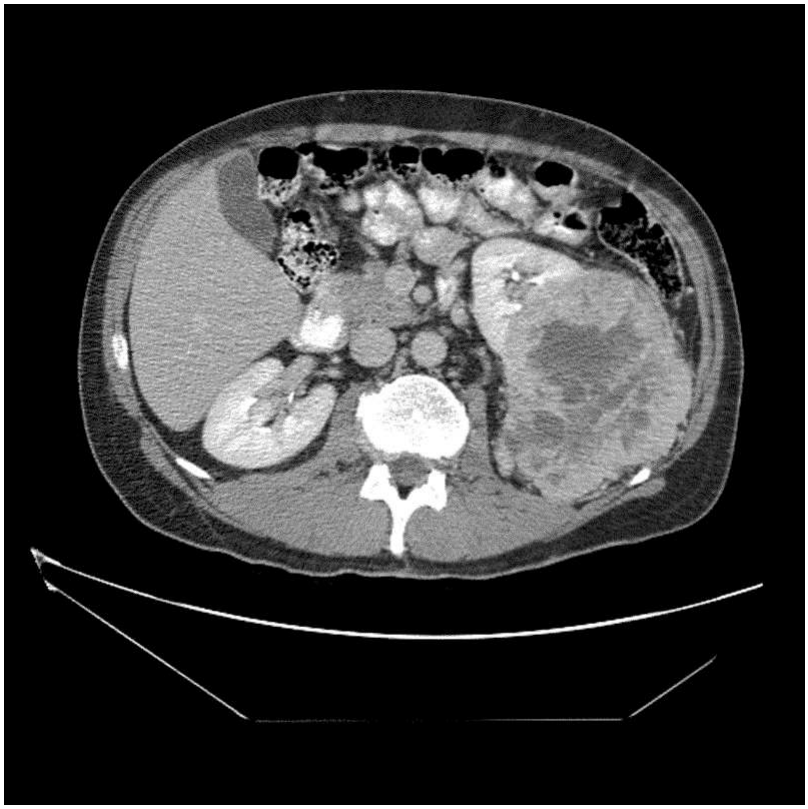
$$\mu_y = \sum_j j \sum_i p(i, j)$$

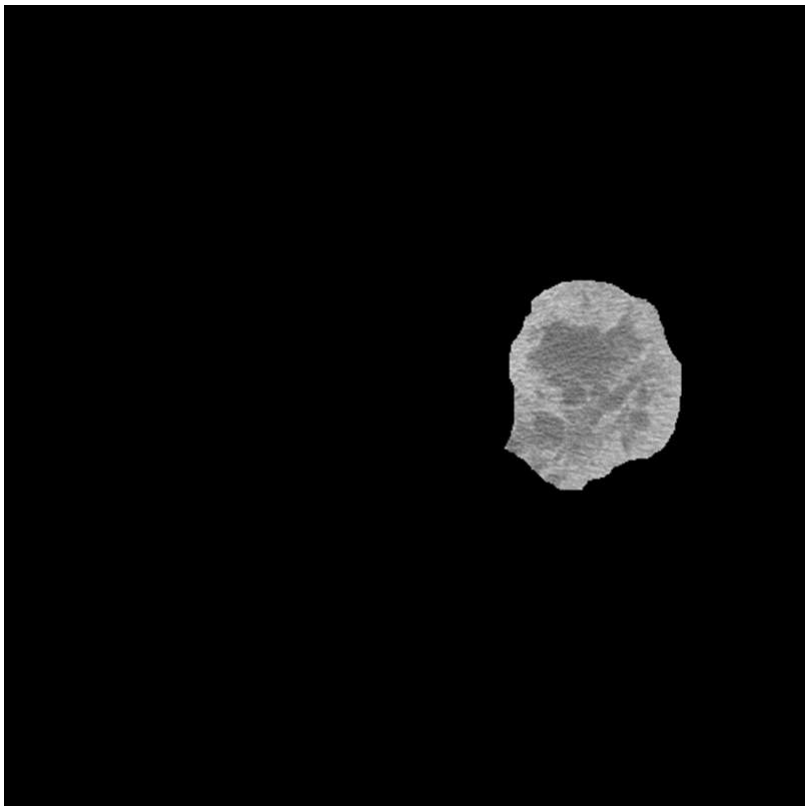
$$\sigma x = \sum_i (i - \mu_x)^2 \sum_j p(i, j)$$

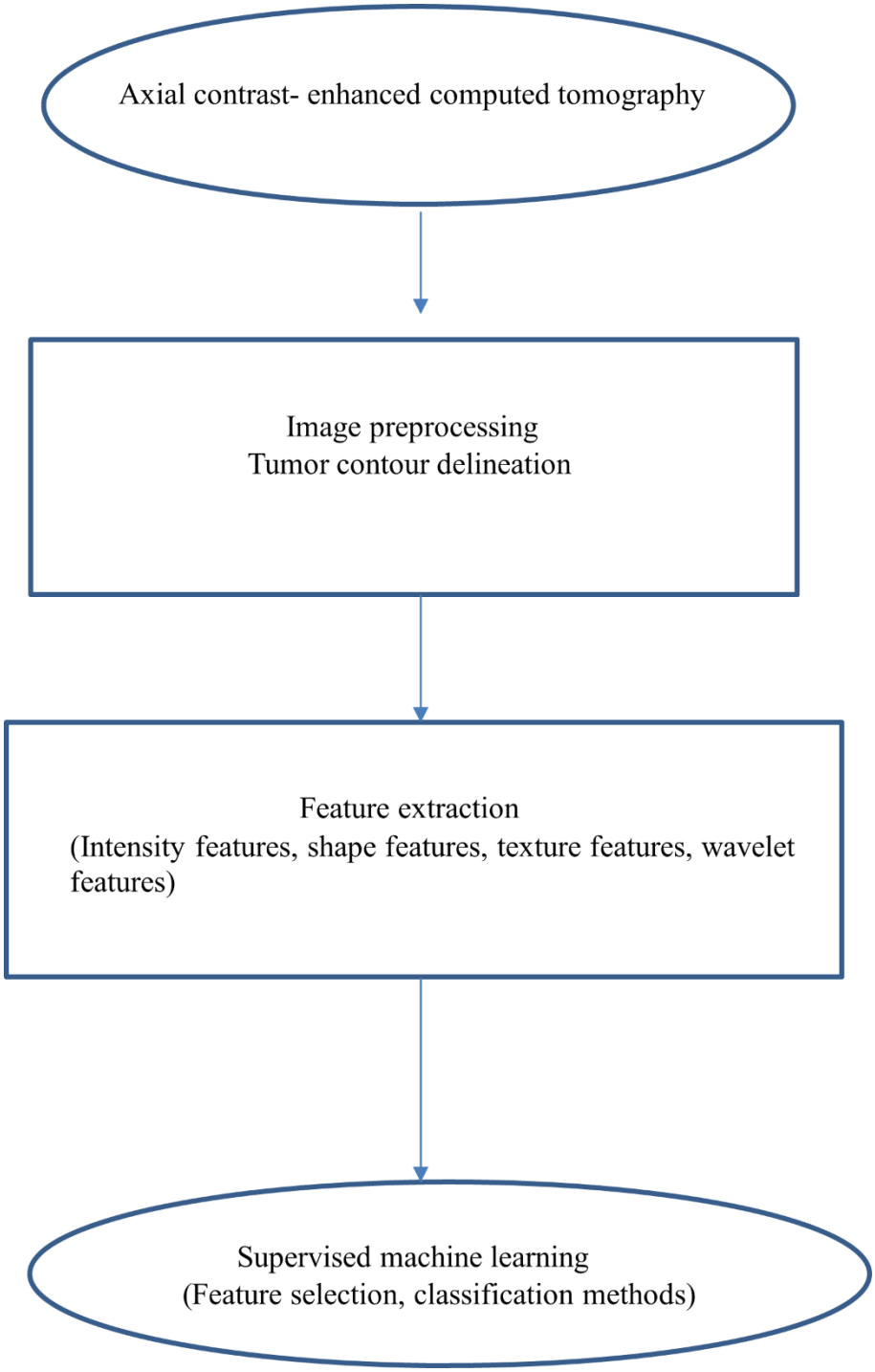
$$\sigma y = \sum_j (j - \mu_y)^2 \sum_i p(i, j)$$

For Gabor transformation texture features

C means the wavelength of the sinusoidal factor,
θ *means the orientation of the normal to the parallel stripes of a Gabor function,*
ψ *is the phase offset,*
δ *is the standard deviation of the Gaussian envelope*
γ *is the spatial aspect ratio . and specifies the ellipticity of the support of Gabor function*






Axial contrast- enhanced computed tomography
Image preprocessing
Tumor contour delineation
Feature extraction
(Intensity features, shape features, texture features, wavelet features)
Supervised machine learning
(Feature selection, classification methods)

References

1 Barata, P. C. & Rini, B. I. Treatment of renal cell carcinoma: Current status and future directions. *CA: a cancer journal for clinicians* (2017).

2 Ferlay, J. *et al.* (2014).

3 Leibovich, B. C. *et al.* Prediction of progression after radical nephrectomy for patients with clear cell renal cell carcinoma. *Cancer* **97**, 1663-1671 (2003).

4 Goh, V. *et al.* Assessment of response to tyrosine kinase inhibitors in metastatic renal cell cancer: CT texture as a predictive biomarker. *Radiology* **261**, 165-171 (2011).

5 Haider, M. A. *et al.* CT texture analysis: a potential tool for prediction of survival in patients with metastatic clear cell carcinoma treated with sunitinib. *Cancer Imaging* **17**, 4 (2017).

6 Zigeuner, R. *et al.* External validation of the Mayo Clinic stage, size, grade, and necrosis (SSIGN) score for clear-cell renal cell carcinoma in a single European centre applying routine pathology. *European urology* **57**, 102-111 (2010).

7 Al-Aynati, M. *et al.* Interobserver and intraobserver variability using the Fuhrman grading system for renal cell carcinoma. *Archives of pathology & laboratory medicine* **127**, 593-596 (2003).

8 Bektas, C. T. *et al.* Clear Cell Renal Cell Carcinoma: Machine Learning-Based Quantitative Computed Tomography Texture Analysis for Prediction of Fuhrman Nuclear Grade. *European radiology*, doi:10.1007/s00330-018-5698-2 (2018).

9 Ng, F., Kozarski, R., Ganeshan, B. & Goh, V. Assessment of tumor heterogeneity by CT texture analysis: can the largest cross-sectional area be used as an alternative to whole tumor analysis? *European journal of radiology* **82**, 342-348 (2013).

10 Haghighat, M., Zonouz, S. & Abdel-Mottaleb, M. CloudID: Trustworthy cloud-based and cross-enterprise biometric identification. *Expert Systems with Applications* **42**, 7905-7916 (2015).

11 Sahiner, B. *et al.* Computer-aided characterization of mammographic masses: accuracy of mass segmentation and its effects on characterization. *IEEE transactions on medical imaging* **20**, 1275-1284 (2001).

12 Miles, K. A., Ganeshan, B. & Hayball, M. P. CT texture analysis using the filtration-histogram method: what do the measurements mean? *Cancer Imaging* **13**, 400 (2013).

13 Haralick, R. M. & Shanmugam, K. Textural features for image classification. *IEEE Transactions on systems, man, and cybernetics*, 610-621 (1973).

14 Ilonen, J. *et al.* Image feature localization by multiple hypothesis testing of Gabor features. *IEEE Transactions on Image Processing* **17**, 311-325 (2008).

15 Kamarainen, J.-K., Kyrki, V. & Kalviainen, H. Invariance properties of Gabor filter-based features-overview and applications. *IEEE Transactions on image processing* **15**, 1088-1099 (2006).

16 Bouckaert, R. R. *et al.* WEKA manual for version 3-8-1. *Univ. Waikato*, 341 (2016).

17 Mulders, P. *et al.* Prognostic value of karyometric and clinical characteristics in renal cell carcinoma. Quantitative assessment of tumor heterogeneity. *Cancer* **72**, 2667-2674 (1993).
18 Huhdanpaa, H. *et al.* CT prediction of the Fuhrman grade of clear cell renal cell carcinoma (RCC): towards the development of computer-assisted diagnostic method. *Abdominal imaging* **40**, 3168-3174 (2015).
19 Amarreh, I., Meyerand, M. E., Stafstrom, C., Hermann, B. P. & Birn, R. M. Individual classification of children with epilepsy using support vector machine with multiple indices of diffusion tensor imaging. *NeuroImage: Clinical* **4**, 757-764 (2014).
20 Fukunaga, K. & Mantock, J. M. A nonparametric two-dimensional display for classification. *IEEE transactions on pattern analysis and machine intelligence* **4**, 427-436 (1982).
21 Lubner, M. G., Stabo, N., Abel, E. J., del Rio, A. M. & Pickhardt, P. J. CT textural analysis of large primary renal cell carcinomas: pretreatment tumor heterogeneity correlates with histologic findings and clinical outcomes. *American Journal of Roentgenology* **207**, 96-105 (2016).

Table Legends section

Table 1 Description of extracted features (abbreviation)

Table 2 Significant radiomic features and relevant p values generated by independent sample t test (normal distribution) or Mann Whitney U test (non-normal distribution)

Table 3. Performance of eleven classifiers for prediction of high-grade and low-grade Fuhrman nuclear groups for selected 23 features

Table 4. Equations of computed tomography texture features

F**igure Legends section** –

Figure 1 Representative contoured tumor of transverse view of contrast -enhanced CT images of clear cell RCC from The Cancer Imaging Archive of the National Cancer Institute. The figure is an open-access image distributed under the terms of the Creative Commons Attribution License (CC BY).

Figure 2 represent contoured tumor of transverse view of contrast -enhanced CT images of clear cell RCC from The Cancer Imaging Archive of the National Cancer Institute.

Figure 3. Flowchart of medical image analysis

Graphic abstract. Process of machine learning

Supplementary Files

This is a list of supplementary files associated with this preprint. Click to download.

- IRB5034870relatedms4646880sq33n91.pdf
- commentinRadiomics.docx
- grant5034870relatedms4646879sq33n9.pdf